Magnetic MIL(Fe)-type MOF-derived N-doped nano-ZVI@C rods as heterogeneous catalyst for the electro-Fenton degradation of gemfibrozil in a complex aqueous matrix

Zhihong Ye [a], José A. Padilla [b], Elena Xuriguera [b], Enric Brillas [a], Ignasi Sirés [a],*

[a] *Laboratori d'Electroquímica dels Materials i del Medi Ambient, Departament de Química Física, Facultat de Química, Universitat de Barcelona, Martí i Franquès 1-11, 08028 Barcelona, Spain*

[b] *DIOPMA, Departament de Ciència de Materials i Química Física, Facultat de Química, Universitat de Barcelona, Martí i Franquès 1-11, 08028 Barcelona, Spain*

Corresponding author: E-mail address: i.sires@ub.edu (I. Sirés)

Abstract

The application of metal-organic frameworks (MOFs) as suspended heterogeneous catalysts in electro-Fenton (EF) process for water treatment is almost inexistent. Fe-MOFs synthesized from phthalic acid-based linkers were spindle-shaped MIL(Fe)-88B and NH_2-MIL(Fe)-88B crystals, whereas their calcination yielded nano-ZVI@C and nano-ZVI@C-N. The lipid regulator gemfibrozil was spiked into 0.050 M Na_2SO_4 solutions or urban wastewater and treated in electrolytic cells with an air-diffusion cathode to generate H_2O_2. The nano-ZVI@C-N catalyst obtained at 800 ºC showed the highest activity, with high stability as deduced from the low iron leaching and high recyclability. Almost total drug removal and significant mineralization was feasible in both matrices at near-neutral pH. The presence of core-shell nano-ZVI and Fe_3O_4 nanoparticles encapsulated in N-doped fusiform porous carbon rods was revealed, ensuring the Fe(III) conversion to Fe(II). Carbon doping with N contributed to the enhanced catalytic activity, and the strong magnetism facilitated the post-treatment catalyst recovery.

Keywords: Electro-Fenton; Gas-diffusion electrode; Metal-organic framework; Pharmaceutical; Water treatment

1. Introduction

Pharmaceutical residues have become one of the main targets among waterborne organic micropollutants, owing to their negative impact on the aquatic ecosystems [1]. They are present in all kinds of water streams, and their potentially deleterious effects on the fauna have been recognized [2]. Pharmaceuticals are ubiquitous in urban wastewater treatment plant (WWTP) influents, being discharged to surface water because of their poor biodegradation and sorption to sludge [3], as well as the low effectiveness of the current tertiary treatments to prevent their accumulation in the plant effluents [4-6]. Consequently, there exist a global consensus on the need for protection of humans and ecosystems from pharmaceutical pollution [7].

Much research is now focused on the development of more effective technologies that allow a proper management of urban wastewater, ensuring the complete degradation of such contaminants before discharge. The electrochemical advanced oxidation processes (i.e., electrochemical AOPs) offer a range of potentially viable technologies for this purpose [8-10]. Among them, the electro-Fenton (EF) process is particularly appropriate because it combines two key characteristics [11,12]: (i) it ensures the fast and complete destruction of the drug molecules, thanks to the massive production of a powerful oxidant like free hydroxyl radical ($^{\bullet}OH$) in the bulk solution via Fenton's reaction (1); and, (ii) unlike the conventional Fenton process [13], the H_2O_2 needed as reactant is produced on site from the cathodic O_2 reduction reaction (2) [14-18], thus becoming a safer, cheaper and more eco-friendly alternative.

$$Fe^{2+} + H_2O_2 \rightarrow Fe^{3+} + {}^{\bullet}OH + OH^- \tag{1}$$

$$O_2 + 2H^+ + 2e^- \rightarrow H_2O_2 \tag{2}$$

Furthermore, the anode (M) contributes to the generation of adsorbed hydroxyl radicals from reaction (3) and, in the presence of Cl^-, to chlorine production via reaction (4) [19-21]:

$$M + H_2O \rightarrow M({}^{\bullet}OH) + H^+ + e^- \tag{3}$$

53      $M + 2Cl^- \rightarrow M + Cl_{2(aq)} + 2e^-$ (4)
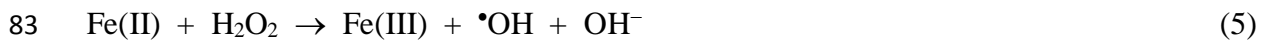
54   Nonetheless, the main drawback for the deployment of homogeneous EF at larger scale is

55 its restriction to acidic pH, in order to prevent the precipitation of the iron catalyst, with the

56 consequent efficiency loss [11,12]. This is not compatible with urban wastewater effluents,

57 whose pH is near neutral [22], which has fostered the recent development of heterogeneous EF

58 although most of the investigation has been made with model solutions [23,24]. The

59 performance of this process depends on the ability of the catalyst to generate $^•OH$ from

60 heterogeneous Fenton's reaction (5). Several materials have been employed as heterogeneous

61 catalysts in EF, including: synthetic iron-loaded structures, such as carbon nanotubes [25],

62 resins [26], zeolites or biosorbents [12]; waste materials like fly ash; zero-valent ion (ZVI) [23];

63 iron-rich soils (like clays) [27]; and minerals like iron oxides or pyrite [14,28]. However, it is

64 unusual that these materials combine a high catalytic activity, stability and recyclability. In

65 general, most of them lose some of their active sites during the treatment and suffer from

66 excessive iron leaching. Excessive solubilization is highly detrimental because of the structural

67 modification of the catalyst and the iron precipitation. This phenomenon requires sludge

68 management after treatment, which would be costly and time consuming at industrial scale.

69   Within this context, metal-organic frameworks (MOFs) have appeared as potentially

70 superior materials. MOFs are highly ordered and porous crystalline structures synthesized from

71 metal ion/clusters and multidentate organic ligands. They might allow overcoming some

72 current technical limitations, showing good perspectives for industrial applications [29], in

73 particular for adsorption, filtration and degradation of organics in water [30]. Their appeal

74 originates from the large porosity and chemical tunability, beneficial for adsorption, which adds

75 to their particular catalytic nature as recently verified in MOF-catalyzed AOPs [31].

76   The use of iron-MOFs, either as ready-to-use materials or as precursors of Fe/C hybrids

77 (i.e., MOF-derived materials), as catalysts for non-electrochemical Fenton-like process has

78   received increasing attention due to their permanent porosity and tunable open metal centers.

79   This favors the conversion of Fe(III) to Fe(II) active sites [32], which is crucial to maintain the

80   continuous $^{\bullet}$OH production from reaction (5) since, otherwise, the accumulation of Fe(III)

81   causes the partial consumption of H_2O_2 through the competitive heterogeneous Fenton-like

82   reaction (6) that yields the weaker oxidant hydroperoxyl radical ($HO_2^{\bullet}$).

83     $Fe(II) + H_2O_2 \rightarrow Fe(III) + {}^{\bullet}OH + OH^-$ (5)

84     $Fe(III) + H_2O_2 \rightarrow Fe(II) + HO_2^{\bullet} + H^+$ (6)

85   In contrast, the application of MOFs to EF process is much more incipient. They have never

86   been employed as suspended catalysts, and only a reduced number of articles have reported the

87   use of MOF-modified cathodes [33-35]. Among the latter group, Le et al. [36,37] have

88   described the successful preparation of carbon-felt cathode modified with a Zn-MOF (i.e., ZIF-

89   8), whose subsequent carbonization enhanced the degradation of Acid Orange 7 dye by EF

90   process. The series of iron-based MILs (Materials from Lavoisier Institute, also called MIL(Fe)-

91   type MOFs) prepared from Fe(III) and terephthalic acid, like MIL(Fe)-53, MIL(Fe)-88 and

92   MIL(Fe)-101, seems particularly promising for the destruction of organic pollutants, as

93   demonstrated in conventional Fenton process with MIL(Fe)-88B as catalyst [38]. However, the

94   direct use of most Fe-MOFs as catalysts is restricted due to their self-decomposition in water.

95   Therefore, MOF-derived metal@carbon composite materials, i.e., metal nanoparticles

96   encapsulated in porous carbon, have been recently developed by pyrolysis of MOFs in inert

97   atmosphere. Under such conditions, the carbonization of the organic polymers is induced and

98   the resulting highly porous carbon is beneficial to minimize the mass transport limitations.

99   Simultaneously, metal precursors are converted into metal nanoparticles [39]. The obtention of

100   nanosized MOFs is interesting, aiming to increase the catalytic performance, but it complicates

101   the post-treatment recovery. Hence, calcination may have an additional role as a method to

102   produce magnetic materials [40-45]. Worth considering, nitrogen can be incorporated as

103 heteroatom into the framework when amine-containing linkers are employed, enhancing the

104 activity and stability [46,47].

105   This work addresses the synthesis of MIL(Fe)-type and NH_2-MIL(Fe)-type MOFs, along

106 with the corresponding calcined magnetic materials. Their thorough characterization informed

107 about their properties and, subsequently, they were employed as catalysts in heterogeneous EF

108 treatment of gemfibrozil spiked into 0.050 M Na_2SO_4 solutions or into urban wastewater.

109 Gemfibrozil is one of the most frequently detected blood lipid regulators in water [48], being

110 considered a high priority pharmaceutical by the Global Water Research Coalition [49]. Since

111 its removal rate in WWTPs is only around 50% [50], it has been detected in groundwater [51]

112 and rivers [49], showing a large persistence. It can affect negatively to aquatic organisms [51],

113 acting as a peroxisome proliferator, and its high estrogenic activity has been shown [52,53].

114 Gemfibrozil solutions have been treated by conventional Fenton [54] and photo-Fenton [55] at

115 pH 5.0, as well as by UVC and UVC/H_2O_2 [56]. Regarding the electrochemical AOPs, uniquely

116 the performance of electro-peroxone [57] and electro-oxidation with electrogenerated H_2O_2

117 (EO- H_2O_2) with a BDD anode has been investigated [58], whereas EF treatment has not been

118 attempted so far. In this study, the degradation products have been identified and the involved

119 mechanism has been proposed. EF was also applied to the degradation of mixtures of

120 gemfibrozil with other pharmaceuticals.

121 **2. Materials and methods**

122 *2.1. Chemicals*

123   Gemfibrozil ($C_{15}H_{22}O_3$, 250.33 g mol^{-1}, CAS No. 25812-30-0, pure) and 5,5-dimethyl-1-

124 pyrroline-N-oxide (DMPO, CAS No. 3317-61-1, $\geq$ 97%) were purchased from Sigma-Aldrich

125 and used as received. Sodium sulfate (CAS No. 7757-82-6, $\geq$ 99%), hydrochloric (CAS No.

126 7647-01-0, 37%) and sulfuric (CAS No. 7664-93-9, 95-97%) acids, and sodium hydroxide

127   (CAS No. 1310-73-2, $\geq$ 98%) were acquired from Merck. The reagents for the synthesis of

128   MOFs were $FeCl_3 \cdot 6H_2O$ from Panreac (CAS No. 7705-08-0, 97%), terephthalic acid (1,4-

129   benzenedicarboxylic acid, i.e., H_2-BDC, CAS No. 100-21-0, 98%) or 2-aminoterephthalic acid

130   (NH_2-BDC, CAS No. 10312-55-7, 99%) from Sigma-Aldrich, and N,N-dimethylformamide

131   (DMF, CAS No. 4637-24-5, pure) from Sigma-Aldrich. Ethanol (CAS No. 64-17-5, > 99%)

132   and methanol (CAS No. 67-56-1, 99.5%) were from Panreac. $TiOSO_4$ (CAS No. 13825-74-6,

133   $\geq$ 29% of Ti as TiO_2) and H_2O_2 (CAS No. 7722-84-1, 30% w/w) were from Sigma-Aldrich and

134   Panreac, respectively. 1,10-Phenantroline monohydrate (Alfa-Aesar, CAS No. 5144-89-8, $\geq$

135   99%), $(NH_4)_2Fe(SO_4)_2 \cdot 6H_2O$ (Panreac, CAS No. 7783-85-9, pure) and ascorbic acid (Sigma-

136   Aldrich, CAS No. 50-81-7, $\geq$ 99%) were employed to determine the dissolved iron

137   concentration. Organic solvents of HPLC or analytical grade were purchased from Panreac and

138   Merck. All aqueous solutions for analyses, as well as synthetic gemfibrozil solutions, were

139   prepared with Millipore Milli-Q water (ρ > 18.2 MΩ cm).

140   Some performance tests were made by spiking gemfibrozil into the secondary effluent from

141   an urban wastewater treatment plant, whose general parameters were (with a relative error of

142   1% for concentrations): 73.2 mg C L^{-1} of total carbon, 13.4 mg C L^{-1} of total organic carbon

143   (TOC), 16.7 mg N L^{-1}, 2.1 mS cm^{-1}, pH 7.5; anions: 181 mg L^{-1} SO_4^{2-}, 535 mg L^{-1} Cl^- and 61.4

144   mg L^{-1} NO_3^-; cations: 555 mg L^{-1} Na^+, 51.4 mg L^{-1} K^+, 103 mg L^{-1} Ca^{2+}, 37.3 mg L^{-1} Mg^{2+} and

145   0.09 mg L^{-1} Fe^{3+}. Prior to storage at 4 ºC, the sample was acidified and the dissolved CO_2 was

146   air-stripped. Before running the degradation trials, the solution pH was adjusted to 7.0 with a

147   concentrated NaOH solution.

148   *2.2. Synthesis procedure*

149   To synthesize the MIL(Fe)-type MOF, $FeCl_3 \cdot 6H_2O$ and H_2BDC (5 mmol of each reactant)

150   were mixed and dissolved in 25 mL DMF, and then stirred for 20 min to get a homogeneous

151   solution. Subsequently, the mixture was poured into a 100 mL Teflon-lined stainless steel

152 autoclave, which was placed in a fan oven preheated to 110 °C and kept for 24 h. The autoclave

153 was then removed from the oven and cooled down naturally to room temperature, whereupon

154 the powdery product was collected by filtration, sequentially washed with methanol and water,

155 and finally dried overnight in an oven at 80 °C. The resulting powder was stored at room

156 temperature in a covered glass container. The same procedure was followed to synthesize the

157 NH$_2$-MIL(Fe)-type MOF, but replacing H$_2$BDC by NH$_2$-BDC. Nano-ZVI@C and nano-

158 ZVI@C-N (i.e., N-doped) were prepared by annealing the previous MOFs in a tube furnace at

159 the required temperature for 4 h under N$_2$ atmosphere. The two materials were collected via the

160 application of an external magnet, and then washed and dried as described for the non-calcined

161 materials.

162 *2.3. Electrolytic trials*

163   Most of the experiments were carried out under continuous stirring in a one-compartment

164 glass cell, open to atmosphere and thermostated at 35 ºC. Electrolyses were performed at

165 constant current employing an Amel 2053 potentiostat-galvanostat. The cathode was a 3-cm^2

166 carbon-Teflon air-diffusion electrode supplied by BASF, placed in a tubular gas chamber and

167 fed with air pumped at 1 L min^{-1} for continuous H$_2$O$_2$ generation. The 3 cm^2-anode was either

168 a Ti plate coated with IrO$_2$, purchased from NMT Electrodes, or a BDD thin film deposited on

169 a Si wafer, supplied by NeoCoat. The interelectrode gap was 1.0 cm. Before first use of the

170 electrodes, a polarization was run in 150 mL of a 0.05 M Na$_2$SO$_4$ solution at 300 mA for 180

171 min, allowing the conditioning of all their surfaces. All the degradation trials were made with

172 150 mL of 0.050 M Na$_2$SO$_4$ solutions or urban wastewater. The EF treatments were performed

173 in the presence of one of the synthesized catalysts.

174 *2.4. Catalyst characterization*

175   Several techniques were used to analyze the morphological features, structure,

176 composition, size and other relevant properties of the synthesized materials. The morphology

177   was assessed by high resolution transmission electron microscopy (HRTEM), using a JEOL

178   JEM-2100 LaB6 microscope operating at 200 kV in STEM mode with a dark-field detector,

179   and coupled to an Oxford Inca energy-dispersive X-ray spectrometer (EDS). HRTEM analysis

180   with made with the Digital Micrograph software, whereas mapping acquisition was

181   accomplished with the Inca Microanalysis Suite version 4.09 software.

182   Powder X-ray diffraction (XRD) analysis was carried out using a PANalytical X'Pert PRO

183   MPD Alpha-1 powder diffractometer in Bragg-Brentano $\theta/2\theta$ geometry with Cu $K_{\alpha 1}$ radiation

184   ($\lambda = 1.5406$ Å). The 2θ-scans ranged from 4 to 100º, with a step size of 0.017º and measuring

185   time of 150 s. Samples were prepared by pressing of the powdery materials with a glass plate

186   to yield a flat surface.

187   The Fourier-transform infrared (FTIR) spectra were recorded on a Nicolet 6700 FTIR

188   spectrometer (Thermo Scientific), equipped with a smart orbit to directly analyze the powders.

189   Thermogravimetric analysis (TGA) was performed on a Mettler-Toledo TGA-851e

190   thermobalance. The powdery samples were placed in alumina crucibles of 70 µL volume. Dry

191   N_2 was supplied at a flow rate of 50 mL min^{-1}, and the samples were heated from 30 ºC to 900

192   ºC at 10 ºC min^{-1}. A blank curve was previously obtained for signal correction.

193   The specific surface area was determined using the Brunauer–Emmett–Teller (BET)

194   method, where N_2 was used as the adsorbate gas. The data where obtained using a TriStar 3000

195   surface area analyzer from Micromeritics within the range $0.05 \leq P/P_0 \leq 0.25$. Sample

196   outgassing was performed under vacuum at 40 ºC for 4 h.

197   The particle size distribution was measured by dynamic light scattering (DLS), using an

198   LS 13 320 laser diffraction particle size analyzer (Beckman Coulter). The dispersion medium

199   was acetone and the samples were sonicated (30 kHz, 200 W) for 5 min before analysis. The

200   zeta-potential (ξ) of each sample as a function of pH was determined using a Malvern Zetasizer

201   Nano ZS (Micromeritics AUTOCHEM 2920) at room temperature, using the Zetasizer version

202 7.11 software. Buffer solutions at pH values from 3.0 to 7.0 were prepared by mixing different

203 volumes of 0.10 M acetic acid and 0.20 M sodium acetate solutions. The powdery catalyst was

204 suspended in the different buffer solutions using an ultrasonic bath and then, the suspension

205 was introduced in a disposable folded capillary cell (DTS 1070).

206   X-ray photoelectron spectroscopy (XPS) analysis was performed with a PHI 5500

207 Multitechnique System (Physical Electronics) using a monochromatic X-ray source (Al K_α line

208 of 1486.6 eV energy, 350 W), placed perpendicular to the analyzer axis and calibrated using

209 the $3d_{5/2}$ line of Ag with a full width at half maximum (FWHM) of 0.8 eV. The analyzed area

210 was a circle of 0.8 mm diameter and the selected resolution for the spectra was 187.85 eV of

211 Pass Energy (PE) and 0.8 eV/step for the general spectra, and 23.5 eV of PE and 0.1 eV/step

212 for the different elements. The energy electron gun was lower than 10 eV. All measurements

213 were made under ultra-high vacuum at pressures between 5×10^{-9} and 2×10^{-8} Torr. The spectra

214 were analyzed using the ULVAC-PHI MultiPakTM software version 8.2.

215   Fe content of catalysts was analyzed by inductively-coupled plasma with optical detection

216 (ICP-OES) using a Perkin Elmer Optima 3200RL. Digestion of samples (0.0159 g) was carried

217 out in a Milestone Ethos Plus microwave oven, using a high pressure closed Teflon reactor. A

218 temperature program was followed to reach 180 ℃, 210 ℃, 220 ℃ and, finally, 230 ℃,

219 employing HNO_3, HCl and H_2O_2 as oxidizing media. C and N were analyzed using a Thermo

220 EA 1108 elemental organic analyzer (Thermo Scientific) operated under standard conditions:

221 He flow rate of 120 mL min^{-1}, combustion furnace at 1000 ℃, chromatographic column oven

222 at 60 ℃ and oxygen loop of 10 mL at 100 kPa.

223   The magnetic characterization of the claimed catalysts was made on a Quantum Design

224 SQUID MPMS-XL susceptometer. The hydroxyl radicals formed during the EF treatments

225 were detected by spin trapping, analyzing the •OH-DMPO adduct by electron paramagnetic

226 resonance (EPR). To do this, solutions of 75 mL of 10 mM DMPO with 0.050 M Na_2SO_4 at

227   natural pH were electrolyzed at 25 mA. The samples were immediately frozen with dry ice

228   upon withdrawal for preservation, to be further analyzed by EPR using a Bruker ESP300E

229   spectrometer, which was set up as follows: center magnetic field at 3505.09 G, sweep width of

230   100 G, microwave frequency of 9.82 GHz, microwave power of 2.00 mW, modulation

231   amplitude of 1.5 G, time constant of 10.24 ms, conversion time of 81.92 ms and sweep time of

232   83.89 s. Win-EPR and SimFonia version 2.3 software were employed.

233   *2.5. Other instruments and analytical methods*

234   The specific conductivity of solutions was determined from measurements made with a

235   Metrohm 644 conductometer, whereas their pH was measured on a Crison GLP 22 pH-meter.

236   All the samples were microfiltered (0.45 μm, Whatman syringe filters) prior to any analysis.

237   The time course of H_2O_2 concentration was assessed from the absorption ($\lambda = 408$ nm) of its

238   yellow complex with Ti(IV), obtained on a Shimadzu 1800 UV/Vis spectrophotometer at room

239   temperature. The dissolved Fe^{2+} concentration was obtained by measuring the absorption of the

240   reddish solutions resulting upon its complexation with 1,10-phenantroline, whose maximum

241   absorbance was at $\lambda = 510$ nm. Some samples were also measured by ICP-OES using an Optima

242   3200L spectrometer (Perkin Elmer).

243   Each degradation trial was carried out twice, and the averaged values are depicted in the

244   corresponding figures, along with the error bars with 95% confidence interval. TOC from

245   solutions was determined on a Shimadzu TOC-VCNS analyzer, using the non-purgeable

246   organic carbon method that yielded reproducible TOC values with ±1% accuracy. TN was

247   determined on a Shimadzu TNM-1 unit coupled to the same analyzer. Gemfibrozil

248   concentration was analyzed by reversed-phase high performance liquid chromatography

249   (HPLC) using a Waters 600 chromatograph coupled to a Waters 996 photodiode array detector

250   set at 276 nm. A BDS Hypersil C18 5 μm (250 mm × 4.6 mm) column at 35 ºC was fitted in

251   the equipment. The mobile phase was a 60:40 (v/v) CH_3CN/10 mM KH_2PO_4 (pH 3.0) mixture

252 eluted at 1.0 mL min⁻¹, and the peak of gemfibrozil was obtained at 11.4 min. Samples were

253 always diluted with CH_3CN to stop the drug degradation, and the concentration values reported

254 here have a relative error of 1%.

255   Gas chromatography coupled to mass spectrometry (GC-MS) performed in a 6890N gas

256 chromatograph (Agilent Technologies) coupled to a 5975C mass spectrometer operating in

257 electron impact mode at 70 eV allowed the identification of reaction products. A nonpolar

258 Teknokroma Sapiens-X5ms and a polar HP INNOWax column, both of 0.25 μm (30 m × 0.25

259 mm), were used. The initial temperature was 36 ℃ for 1 min, which was increased up to 320

260 ℃ at 5 ℃ min⁻¹. The temperature of the inlet, source and transfer line was 250, 230 and 300

261 ℃, respectively. CH_2Cl_2 allowed the extraction of the organics from the aqueous samples,

262 yielding an organic solution that was dried over anhydrous Na_2SO_4. After filtration, it was

263 concentrated under a gentle N_2 stream. The mass spectra were compared to those found in the

264 NIST05 MS database.

265 **3. Results and discussion**

266 *3.1. Characterization of the synthesized catalysts*

267   Fig. 1 collects the powder XRD patterns of the four synthesized catalysts, namely two raw

268 MOFs and two MOF-derived materials. In Fig. 1a, it can be observed that the diffractograms

269 of the as-synthesized MIL(Fe)-type and NH_2-MIL(Fe)-type MOFs exhibit numerous diffraction

270 peaks. Most of them are thin, revealing the high crystallinity of both materials. The main peaks

271 (and the corresponding planes) for the former MOF appear at 9.3º (101), 9.5º (002), 12.5º (102),

272 13.9º (100), 16.1º (200), 16.4º (103), 16.5º (112), 18.8º (202) and 21.9º (211). The N-rich MOF

273 presents a similar pattern, although those peaks tend to be shifted to slightly lower angles (when

274 they are present) and some additional peaks can be seen. They appear at 7.5º (100), 8.2º (101),

275 9.4º (002), 12.2º (102), 18.0º (202) and 21.7º (212). In both cases, the values show a good

276 agreement with the characteristic patterns of MIL(Fe)-88B and NH$_2$-MIL(Fe)-88B [59], rather

277 than those expected for MIL(Fe)-53 (and NH$_2$-MIL(Fe)-53) [60] or MIL(Fe)-101 (and NH$_2$-

278 MIL(Fe)-101) [61] that are also prepared from FeCl$_3$ and H$_2$BDC (or NH$_2$-BDC) mixtures.

279   Fig. 1b shows the diffractograms of the nano-ZVI@C and nano-ZVI@C-N catalysts

280 obtained upon calcination of the corresponding MOFs at 800 ºC. The peaks at ~45º, ~65º and

281 ~82º can be attributed to (110), (200) and (211) planes of nano-ZVI (JCPDS Ref. N. 87-0721).

282 The cubic structure of Fe$_3$O$_4$ (JCPDS Ref. N. 65-3107) accounts for the peaks at 30.0º (220),

283 35.5º (311), 43.2º (400), 57.2º (511) and 62.6º (440). The presence of nanoscale ZVI (i.e., nano-

284 ZVI, Fe^0) and iron oxide like Fe$_3$O$_4$ suggests that the porous frameworks of MIL(Fe)-88B and

285 NH$_2$-MIL(Fe)-88B collapsed upon pyrolysis and yielded nanosized reduced and oxidized Fe-

286 based nanoparticles. The formation of nano-ZVI [45] or Fe$_3$O$_4$ [62] upon carbothermal

287 reduction has also been reported considering other reactants.

288   Note that the presence of nitrogen enhanced all the peaks related to ZVI, which means that

289 N-doped carbon behaved as a better reducing agent. This agrees with Liu et al. [47], who

290 reported the increased encapsulation of Fe^0 in the porous carbon upon incorporation of NH$_2$-

291 group to the organic precursor. In contrast, the peaks attributed to magnetite are analogous in

292 both carbonized materials.

293   Based on the good perspectives of the nano-ZVI@C-N catalyst (800 ºC), resulting from

294 the presence of porous carbon, N-doping and more abundant ZVI nanoparticles as compared to

295 the nano-ZVI@C, its characterization was more extensive. The elemental analysis yielded a

296 content of 51.5% Fe, 34.6% C, 11.8% O and 2.15% N. Its zeta-potential decreased as the pH of

297 the tested solutions was higher, yielding an isoelectric point at pH 5.4, which suggests that its

298 surface is negatively charged at a more alkaline pH.

299   Fig. S1 of Supplementary Material shows the FTIR spectra of the four materials, which

300 inform about the surface functional groups. Sharp peaks for the MIL(Fe)-type and NH$_2$-

301   MIL(Fe)-type MOFs within the region of 1600–1400 cm^{-1} can be associated to the

302   asymmetrical and symmetrical stretching modes of the O–C–O framework, which is typical in

303   Fe-MOFs [43]. In addition, the characteristic peak at 540 cm^{-1} can be related to the Fe–O

304   stretching mode in both MOFs, as expected from the link between Fe atoms and the organic

305   ligand. The bands at 3456 cm^{-1} and 3373 cm^{-1} are ascribed to the asymmetrical and symmetrical

306   stretching modes of the amine groups, respectively. The presence of N is also confirmed from

307   the peaks at 1626 cm^{-1} and 1337 cm^{-1}, corresponding to N–H and C–N bonds, respectively.

308   After carbonization under N$_2$ atmosphere, all the peaks disappeared, which corroborates

309   the complete decomposition of the organic ligands to yield porous carbon and the

310   transformation of the iron species mainly into Fe^0, as observed in the XRD patterns.

311   Fig. S2a shows the XPS general spectrum for the nano-ZVI@C-N catalyst (800 ºC). The

312   XPS spectrum of each element present in the catalyst (C 1s, Fe 2p, N 1s and O 1s) is shown in

313   Fig. S2b-e. The C 1s band could be deconvoluted into four peaks centered at 284.5, 285.4, 286.6

314   and 289.4 eV, assigned to C–C, C=N, C–N and O–C=O functional groups, respectively [63].

315   The latter one is actually small, which can be related to the minor oxidation of the porous carbon

316   at the high carbonization temperature. In the spectrum of Fe, the Fe 2p$_{3/2}$ band contains peaks

317   for Fe(II) and Fe(III) at 710.7 and 712.8 eV, respectively, whereas the Fe 2p$_{1/2}$ band contains

318   Fe(II) and Fe(III) at 724.2 and 726.8 eV [47,63]. These peaks confirm the presence of Fe$_3$O$_4$ in

319   the calcined catalyst. In addition, the signal at 719.7 eV can be related to Fe^0 [64]. The N 1s

320   spectrum could be deconvoluted into five peaks [63]: pyridinic N at 398.3 eV, FeN$_x$ at 399.4

321   eV, graphitic N at 400.7 eV, quaternary N at 401.7 eV and oxidized N (i.e., N–O) at 404.2 eV.

322   Alternatively, the peak at 399.4 eV can be associated to pyrrolic N [47]. This variety arises

323   from cyclization reactions, which favor the incorporation of N atoms to carbon rings. The

324   formation of quaternary N was promoted by iron at the high calcination temperature. Finally,

325   Fig. S2e shows the peaks at 531.4 and 533.2 eV, which may be assigned to oxygen vacancies

326 and C–O bonds on the carbon surface, respectively. The peak at 530.1 eV is typical of metal-

327 oxygen bonds, in agreement with the presence of Fe_3O_4 [47].

328   TEM analysis was performed for the as-synthesized MOFs and the calcined catalysts, and

329 the images and elemental mapping for the nano-ZVI@C-N catalyst (800 ℃) can be observed

330 in Fig. 2. The morphological characterization reveals that, after NH_2-MIL(Fe)-88B was

331 carbonized, its typical hexagonal rod-like shape was still preserved, as can be seen in Fig. 2a

332 (highlighted in red). Some authors describe it as a needle-like morphology [38], although it is

333 more convenient to consider it a spindle [39] or a fusiform rod. A shown in the magnified rod

334 in Fig. 2b, some of these structures appeared as truncated carbonaceous rods although, in

335 general, they showed a uniform size of 3.0-4.0 µm in length and 1.0-1.5 µm in width. In

336 addition, iron atoms from the MOF precursor aggregated into quite spherical nanoparticles

337 embedded in the microporous carbon matrix. Two types of particles can be distinguished: big

338 ones (500-600 nm in diameter, in blue) and small ones (150 nm in diameter, in green). Such

339 iron encapsulation is expected to contribute to the minimization of the erosion of nano-ZVI and

340 magnetite, as well as to avoid the precipitation of iron ions on the nanoparticle surface. Fig. 2c

341 evidences the core-shell structure of these particles, which according to the color image shown

342 in Fig. 2d accounts for a carbon shell that surrounds a core composed of either nano-ZVI or

343 Fe_3O_4 (in agreement with the XRD pattern). The elemental mapping of one of the rods, selected

344 as the site of interest in Fig. 2e, confirmed the distribution of elements: Fe and O match quite

345 perfectly with the particle sites, whereas C and N show a uniform distribution along the whole

346 rod, thus confirming the N-doping of carbon mentioned in the XPS analysis. Note that the colors

347 in Fig. 2e are not related to those in Fig. 2d.

348   In order to complete the microscopic study, the HRTEM analysis of the core-shell

349 nanoparticle shown in Fig. 2c was carried out. Fig. S3a points out the region where the selected

350 area electron diffraction (SAED) analysis was performed. The SAED pattern of Fig. S3b

351 evidences the high crystallinity of the core, in agreement with the findings from XRD analysis

352 discussed in Fig. 1. In addition, a high resolution image of the carbon-shell can be seen in Fig.

353 S3c. The magnification of Fig. S3d clearly shows the crystal planes, resulting in a d-spacing of

354 3.98 Å. This value is close to those reported for the (002) plane of carbons prepared by steam

355 pyrolysis at 600-800 ºC, i.e., 3.87-3.93 Å [65], and higher than 3.35 Å expected for graphitic

356 carbon [65].

357 The magnetic properties of the nano-ZVI@C-N catalyst synthesized at 800 ºC, which is a

358 very relevant aspect for practical application, were also assessed. Fig. 3 shows the

359 magnetization curve, showing the typical hysteresis loop that characterizes the ferromagnetic

360 materials at room temperature. The saturation magnetization (M_s) was 66.7 emu g^{-1}, which is

361 higher than those of Fe_3O_4 nanoparticles (44 emu g^{-1}) [66] and Fe_3O_4/carbon composites

362 derived from MIL(Fe)-101 (61.7 emu g^{-1}) [42], and it can be associated to the contribution of

363 abundant nano-ZVI. The M_s of ZVI nanoparticles is 93.0 emu g^{-1} [67], greater than that of our

364 material, as expected from the shielding effect of the porous carbon. Nonetheless, the

365 magnetism of the synthesized material is strong enough for efficient post-treatment magnetic

366 recovery of the catalyst particles using a permanent magnet or an external magnetic field. Worth

367 mentioning, the hysteresis loop was small, exhibiting an almost perfect sigmoidal shape. Hence,

368 the nano-ZVI@C-N catalyst showed a ferromagnetic behavior but approaching to

369 superparamagnetic, since the coercive field is close to zero (i.e., only 200 Oe). The inherent

370 magnetization of the material was possible due to the nanometric dimensions of the iron

371 particles, since the large surface area exposed allow that the spin of the electrons of surface

372 atoms aligns readily in response to even weak magnetic fields, thus simplifying its separation

373 after use.

374 As can be seen from the N_2 adsorption/desorption isotherms depicted in Fig. S4a, the BET

375 surface area of the nano-ZVI@C-N catalyst was much higher than that of its NH_2-MIL(Fe)-

type MOF, yielding values of 216.9 and 56.4 m^2 g^{-1}, respectively. This confirms the large porosity conferred to the N-doped carbon rod upon pyrolysis at 800 ℃. The surface area of the calcined material is higher than that reported for MIL(Fe)-88A-derived carbon rods (i.e., 84.0 m^2 g^{-1}) [41] and within the range of that achieved for materials derived from NH_2-MIL(Fe)-88B (160.0 m^2 g^{-1}) [39], which is potentially beneficial to favor the exposure of active sites and the adsorption of the organic pollutants. On the other hand, the size reduction upon calcination is evident from DLS analysis of Fig. S4b, with mean values decreasing from 200 nm to 90 nm, in agreement with the collapse of the 3D framework. Furthermore, the size distribution became narrower, thus confirming the uniformity of the structural dimensions mentioned from Fig. 2.

In order to elucidate the transformation steps that occur during the pyrolytic process, the TGA curve of the as-synthesized NH_2-MIL(Fe)-type MOF was determined, along with that of the NH_2-BDC precursor, as shown in Fig. S5. The crystalline MOF presented an initial weight loss of 22.0% at 50-275 ℃, which can be related to the release of physisorbed solvent molecules (water, methanol and DMF) [40]. The subsequent weight loss, occurring within the temperature range from 275 ℃ to 450 ℃, was larger (30.1%) and can be attributed to the partial decomposition of the organic ligands, as deduced from the trend of NH_2-BDC. In this stage, the residual NH_2-BDC reactant, the NH_2-BDC molecules encapsulated within the porous framework and the structural NH_2-BDC linker were gradually calcined. Above 475 ℃ and up to about 800-850 ℃, the organic molecules completely decomposed, yielding a total weight loss of around 80%. Curve *a* shows the formation of Fe_3O_4 between 450-650 ℃, thereby being transformed into nano-ZVI from 650 ℃.

3.2. Performance of raw and calcined catalysts for gemfibrozil removal

Once confirmed the appealing properties of the raw and, especially, the calcined MOFs at 800 ℃, they were employed for the treatment of gemfibrozil solutions with 0.050 M Na_2SO_4 at natural pH 5.5, using an IrO_2/air-diffusion cell and 0.2 g L^{-1} of powdery material. Fig. 4

highlights that the use of NH_2-MIL(Fe)-type MOF as catalyst in heterogeneous EF at 50 mA

yielded a 57% gemfibrozil concentration decay at 60 min, resulting from the production of $^\bullet OH$

via Fenton's reaction (5) and Fenton-like reaction (6) occurring at the catalyst surface. The

nano-ZVI@C powder exhibited a large adsorption capacity (i.e., in the absence of current

supply), accounting for a 45% drug removal, as could be expected from the porosity

enhancement upon calcination. Worth noting, Fig. 4 shows the apparently poor catalytic

performance of this material, since the degradation percentage achieved in EF (52%) was close

to the value obtained in the absence of current. In both EF treatments, the drug disappearance

was very fast during the first 10 min, reaching almost the maximal degradation, whereupon the

gemfibrozil concentration remained almost constant probably due to the insufficient generation

of $^\bullet OH$ and the consequent accumulation of refractory organic products [9,11]. Surprisingly,

the drug removal by adsorption on the nano-ZVI@C-N catalyst surface was much lower,

attaining only 10% despite its significantly greater BET area mentioned above. This can be

explained by the occurrence of two combined facts at pH 5.5: (i) the catalyst surface was

negatively charged because its zeta-potential determined above was 5.4; and (ii) the gemfibrozil

molecules were predominantly deprotonated, since the drug pK_a is 4.7 [49]. The nano-ZVI@C-

N-catalyzed EF process exhibited a clear superiority as compared to all the other treatments,

yielding an abatement higher than 95% at 60 min. The drug concentration decay agreed with a

constant reaction rate that could be fitted well to a pseudo-first-order kinetics with $k_1 = 0.0659$

min^{-1} (Table 1), which informs about the great catalytic activity of the ZVI and Fe_3O_4

nanoparticles distributed along the N-doped carbon rods. Both typed of Fe-rich particles are

able to promote the formation of Fe(II) in solid state as well as Fe^{2+} in solution. Furthermore,

nano-ZVI fosters the conversion of Fe(III) to Fe(II) on the catalyst surface. The upgrading as

compared to the nano-ZVI@C can be related to the presence of N, which is believed to increase

the catalytic activity by decreasing the carbon bandgap energy [47]. It is thus necessary to

426 emphasize that, under the latter EF conditions, gemfibrozil removal corresponded to drug

427 destruction, not to a simple separation, based on the low adsorption described above, which

428 corroborates the great interest in NH_2-MIL(Fe)-derived catalysts. Finally, the contribution of

429 $EO-H_2O_2$ process to the whole degradation was evaluated in the absence of the powdery

430 materials, revealing that 17% of the drug disappearance could be accounted for by the action of

431 adsorbed $IrO_2(^\bullet OH)$ formed from water oxidation via reaction (3).

432   The EF trial with the nano-ZVI@C-N catalyst was repeated under the above conditions but

433 in the presence of a given radical scavenger. Fig. S6a shows that the use of *p*-benzoquinone had

434 a very mild effect on the time course of the normalized gemfibrozil concentration. The profile

435 and the final destruction percentage at 60 min (90%) were similar to those obtained in the

436 absence of this scavenger, which is known to react quite selectively with superoxide radical

437 $(O_2^{\bullet -})$. The generation of this oxidant should be feasible from Fenton-like reaction (6), as the

438 conjugated base of $HO_2^\bullet$ with pK_a = 4.8-4.9 [11]. It can then be concluded that the Fe(III)

439 conversion to Fe(II) on the calcined N-doped MOF-derived catalyst surface was very effective,

440 thus minimizing the occurrence of reaction (6). In contrast, Fig. S6a also presents the

441 gemfibrozil disappearance in the presence of *tert*-butanol as a selective $^\bullet OH$ scavenger,

442 achieving a final drug removal as low as 32%, which confirms the preponderant role of this

443 radical, mainly formed from heterogeneous Fenton's reaction (5) thanks to the continuous

444 Fe(II) regeneration. The production of $^\bullet OH$ can be corroborated from the EPR signals detected

445 in the absence of radical scavengers, as depicted in Fig. S6b. The use of the nano-ZVI@C-N

446 catalyst provided more intense signals, especially at 30 min of electrolysis, as compared to those

447 obtained in EF with nano-ZVI@C, which is in agreement with the greater catalytic activity

448 described for the N-doped catalyst in Fig. 4.

449   For the best treatment among those summarized in Fig. 4, namely the EF process with

450 nano-ZVI@C-N, Fig. S7 evidences that the solution pH did not change significantly along the

451   electrolysis, only undergoing a slight acidification. This fact contributed to the very low iron

452   leaching from the catalyst surface toward the solution (0.20 mg L^{-1} at 60 min), as illustrated in

453   the same figure. This informs about the great stability of the calcined material, which is a crucial

454   requirement for scale-up. In addition, Fig. S8 demonstrates the high recyclability of the nano-

455   ZVI@C-N catalyst during the same EF treatment after reusing it in five consecutive trials. The

456   reusability was assessed upon simple magnetic recovery of the catalyst from the reaction

457   mixture under an external magnetic field due to their high M_s value. After the fifth trial, it was

458   still possible to attain a 90% of gemfibrozil degradation at 60 min. The loss of performance

459   could be due to the gradual passivation of the nano-ZVI particles by iron oxides, thus causing

460   the partial deactivation of some of the surface active sites. The catalyst was characterized after

461   usage. As shown in Fig. S9a, the catalyst structure did not undergo any substantial modification,

462   since all diffraction peaks matched quite well with those of the as-synthesized catalyst (see also

463   Fig. 1b). TEM images (Fig. S9b and c) also revealed similar features to those described from

464   Fig. 2, in particular the presence of truncated rods and a perfect carbon-shell surrounding the

465   core. Based on this, the aforementioned passivation is not evident, which means that other

466   deactivation mechanisms may be prevalent to explain the performance decay.

467   Since the nano-ZVI@C-N catalyst was the best material to carry out the heterogeneous EF

468   treatment, the effect of the pyrolysis temperature on its performance was investigated. The

469   enhanced properties of the catalyst synthesized at 800 ºC are evident from Fig. 5a, since the

470   drug destruction at 60 min employing the materials prepared by thermal treatment at 650, 700

471   and 900 ºC was only 58%, 69% and 44%, respectively. Fig. 5b shows the corresponding good

472   pseudo-first-order kinetics exhibited by the fastest and slowest EF processes, i.e., those

473   performed with powder prepared at 800 and 900 ºC, respectively. Aiming to clarify why the

474   optimum temperature was 800 ºC, the four as-synthesized catalysts were characterized by XRD.

475   The patterns of Fig. S10 reveal that the relationship between their performance and the nature

476 and abundance of the iron-based structures present in the rods, especially with nano-ZVI, was

477 quite straightforward. The presence of the latter particles, which are essential to ensure the

478 Fe(III) reduction [45,68], was clearly greater when the pyrolysis temperature was increased

479 from 650 to 800 ℃, as deduced from the higher intensity of the peaks, in particular that at ~45°.

480 Worth noting, the accumulation of this iron form at 800 ℃, formed by in-situ reduction on

481 graphitic carbon [47], can be explained by the gradual transformation of FeN_x (present only at

482 650 ℃) and Fe_3O_4 (present at 650 and 700 ℃). At 800 ℃, FeN_x disappeared and the amount of

483 Fe_3O_4 had decreased. As evidenced in Fig. S10, the synthesis at 900 ℃ restricted the formation

484 of nano-ZVI, with the concomitant promotion of Fe_3O_4. This phenomenon can be related to the

485 collapse of the framework with the condensation of polymers and release of gases, yielding an

486 insufficient amount of reducing agent that ended in the excessive oxidation of the iron-based

487 particles [47]. This explanation is thus in good agreement with the pyrolysis mechanism

488 elucidated from TGA data in Fig. S5.

489 *3.3. Heterogeneous EF treatment of gemfibrozil solutions under different conditions*

490 The effect of various experimental parameters, namely pH, applied current and catalyst

491 dosage, on the performance of the heterogeneous EF treatment in 0.050 M Na_2SO_4 solutions

492 was assessed using the nano-ZVI@C-N catalyst synthesized by pyrolysis at 800 ℃.

493 Fig. 6a shows the influence of pH, from 3.0 to 9.0, on gemfibrozil removal. The

494 degradation percentage at any selected electrolysis time declined as the initial pH value became

495 higher. The fastest decay was achieved at pH 3.0, reaching total removal at 30 min, which can

496 be explained by the expected greater iron solubilization that could promote the production of

497 $^\bullet OH$ from homogeneous Fenton's reaction (1) whose optimum pH is ~3.0. This is verified from

498 Fig. S11a, which shows a large accumulation of dissolved iron (8.5 mg L^{-1} at 60 min). None of

499 the other initial pH values allowed the complete disappearance of the drug after 60 min,

500 attaining decays of 95%, 84% and 69% at pH 5.5, 7.0 and 9.0, respectively. The final leached

501   iron in these three trials was very low (0.1-0.2 mg L^{-1}, Fig. S11a), suggesting the relatively high

502   stability of nano-ZVI@C-N at mild pH. This does not preclude the occurrence of some

503   additional iron leaching, not detected because of its precipitation on the catalyst surface,

504   forming a thicker barrier at higher solution pH. Such precipitate could account for the gradually

505   lower performance of the EF process. Note in Fig. S11a that in all cases, the solutions became

506   slight acidified, which can be due to the production of acidic organic products like aliphatic

507   carboxylic acids (see subsection 3.4). Worth highlighting, even the least effective

508   heterogeneous EF treatment (i.e., at pH 9.0) could greatly outperform the EO-H_2O_2 process

509   (Fig. 4).

510   In Fig. 6b, it can be seen that the applied current did not play a crucial role in heterogeneous

511   EF, since very similar final decay rates could be achieved, especially at current values $\geq$ 50 mA.

512   At 60 min, 86%, 95% and 100% gemfibrozil removal was found at 25, 50 and 75 mA,

513   respectively. The total disappearance could be reached after only 45 min at 100 mA. As can be

514   observed in Fig. S11b, in all trials there was an excess of H_2O_2 concentration accumulated in

515   the solution from reaction (2), which became higher as the applied current increased. This

516   means that the current was partially wasted because homogeneous and heterogeneous Fenton's

517   reaction (1) and (5) could not occur more quickly as their rate was limited by the amount of

518   catalyst and/or their own kinetics [11]. On the other hand, a current increase from 25 to 100

519   mA favored the larger production of $IrO_2(^{\bullet}OH)$, although its oxidation power is much lower

520   than that of $^{\bullet}OH$ [16,19], as deduced from Fig. 4.

521   The catalyst dosage had a more important role, since it is the source of Fe(II)/Fe(III) and

522   their aqueous forms, which eventually determine the amount of $^{\bullet}OH$ produced. Fig. 6c shows

523   a gradual enhancement of gemfibrozil removal, from 72% to 83%, 95% and 100% at 60 min as

524   the catalysts concentration was increased from 0.05 to 0.10, 0.20 and 0.30 g L^{-1}. From Fig. 6b

525   and c it can be inferred that, depending on the need, overall drug destruction is feasible either

526   via current increase or via addition of a slightly greater amount of catalyst, thus providing

527   certain flexibility to the technology.

528   　　All the decays of Fig. 6a-c agreed very well with a pseudo-first-order reaction kinetics, and

529   the corresponding k_1-values are summarized in Table 1.

530   　　In Fig. 7, the trend obtained in EF at pH 5.5 and 50 mA using 0.2 g L^{-1} of catalyst (95%

531   gemfibrozil degradation at 60 min) is compared with those resulting from EF trials performed

532   with other anodes and electrolytes with the same specific conductivity. The use of an IrO_2/air-

533   diffusion cell with 0.041 M Na_2SO_4 + 0.009 M $NaHCO_3$ led to a very poor drug removal, only

534   attaining 31% at 60 min due to the inhibitory effect of HCO_3^- that acts as very effective radical

535   scavenger [69]. This anion reacts with $^{\bullet}OH$ and $IrO_2(^{\bullet}OH)$ to form much weaker radicals like

536   $CO_3^{\bullet-}$ [70]. The replacement of the IrO_2-based anode by BDD in sulfate medium was not

537   particularly advantageous. Despite the well-known high oxidation power of this anode [10], the

538   profile of the normalized gemfibrozil concentration was close to that obtained with IrO_2, being

539   only slightly steeper and ending in 100% degradation at 60 min. This small contribution of

540   BDD($^{\bullet}OH$) to the drug disappearance can then be explained by the preponderant role of $^{\bullet}OH$

541   formed from heterogeneous Fenton's reaction (5) [9-11]. In contrast, the use of a RuO_2/air-

542   diffusion cell with 0.025 M Na_2SO_4 + 0.035 M NaCl was able to accelerate the gemfibrozil

543   destruction, allowing the total removal at 45 min. The RuO_2-based anode is able to produce

544   both, $RuO_2(^{\bullet}OH)$ via reaction (3) and, mainly, active chlorine from reaction (4) [10,19].

545   Therefore, chlorination acted in concomitance with $^{\bullet}OH$-mediated oxidation to significantly

546   enhance the removal.

547   　　The ability of the heterogeneous EF process to remove not only the target pollutant but also

548   its degradation products was assessed from TOC analysis in sulfate medium. The previous

549   BDD/air-diffusion cell and a current of 100 mA were employed, since it was expected that quite

550   refractory products could be formed along the electrolysis. As shown in Fig. S12, a substantial

mineralization of 61% was achieved at 360 min, probably remaining in solution some small persistent organic molecules (see below).

3.4. Degradation products of gemfibrozil, performance in urban wastewater and mechanism

A sample withdrawn at 30 min from the solution treated by EF with 0.2 g L^{-1} nano-ZVI@C-N in the BDD/air-diffusion cell containing 0.050 M Na$_2$SO$_4$ at pH 5.5 was analyzed by GC-MS. Six aromatic (**1-7**) and six aliphatic (**8-13**) products were detected, some of them being previously reported during the sunlight-driven photocatalytic treatment of gemfibrozil solutions [71]. Based on the identified products, the degradation route is proposed in Fig. 8. The initial hydroxylation of **1** with simultaneous decarboxylation yielded 5-(2,5-dimethyl-phenoxy)-2-methyl-pentan-2-ol (**2**), whose demethylation along with the oxidation of the alcohol group led to 5-(2,5-dimethyl-phenoxy)-pentan-2-one (**3**). Upon hydroxylation in their position C1, compounds **1**, **2** and **3** were split into benzenic and aliphatic products. Among the former, 2,5-dimethylphenol (**4**) initiated a sequence that successively produced 2-hydroxy-4-methyl-benzaldehyde (**5**), as well as its monohydroxylated and dihydroxylated derivatives (**6** and **7**, respectively). On the other hand, the release of the side chain of **1** was identified as 2,2-dimethyl-pent-4-enal (**8**), which was transformed into 2,2-dimethyl-pent-4-enoic acid (**9**). This could then yield wither 2-methyl-penta-2,4-dien-1-ol (**10**) or 2-methylacrylic acid (**11**), whereas the side chain of **2** was clearly identified as 4-methyl-pentane-1,4-diol (**12**), which was converted to 4-methyl-pentan-1-ol (**13**). Note that the accumulation of the aliphatic products may explain the partial TOC abatement described in Fig. S12, and accounts for the progressive detoxification of the treated solutions [9-12].

The results discussed so far allow envisaging good perspectives for heterogeneous EF catalyzed with calcined NH$_2$-MIL(Fe)-88B-type MOF, although the trials were made in model matrices. As a step forward to demonstrate the viability of the new system, a more complex aqueous matrix was considered. Four ubiquitous micropollutants, namely gemfibrozil,

naproxen, fluoxetine and bisphenol A, were spiked into urban wastewater at pH 7.0 (each at 10

mg L^{-1} C). The RuO_2/air-diffusion cell was employed, in order to take advantage of it larger

ability to remove gemfibrozil thanks to the production of active chlorine (Fig. 7). In Fig. 9, the

95% disappearance of gemfibrozil at 60 min, along with the total removal of the other three

compounds is evidenced. The slower concentration decay of gemfibrozil as compared to the

trial performed in sulfate/chloride medium described above can be accounted for by the

presence of organic molecules that compete to react with $^\bullet OH$, $RuO_2(^\bullet OH)$ and ClO^-, i.e., the

other three pollutants and, mainly, the natural organic matter (NOM).

Based on the complete set of results obtained in this work, the mechanism of Fig. 10 is

proposed for the nano-ZVI@C-N-catalyzed heterogeneous EF treatment of gemfibrozil

solutions at mild pH. The main oxidants are hydroxyl radicals, which can be formed via: (i)

heterogeneous Fenton process through reaction between cathodically generated H_2O_2 and Fe(II)

on the catalyst surface; (ii) homogeneous Fenton's reaction upon iron leaching; and (iii) H_2O_2

reduction on the N-doped carbon rods. In addition, active chlorine and M($^\bullet OH$) produced via

anodic reactions can contribute to the degradation as well. The nano-ZVI and Fe_3O_4

nanoparticles present in the rods ensured the supply of Fe(II)/Fe(III), being nano-ZVI the main

responsible for the continuous Fe(II) regeneration. The presence of N-doped porous carbon

upgraded the electron transfer that promoted this kind of reaction, eventually enhancing the

catalytic activity.

4. Conclusions

This investigation demonstrates that it is feasible to degrade gemfibrozil, as well as other

typical organic micropollutants, in urban wastewater at mild pH by heterogeneous EF process

using a calcined NH_2-MIL(Fe)-88B MOF as catalyst. At 60 min, 95% drug removal was

achieved in a RuO_2/air-diffusion cell at 50 mA thanks to the action of $^\bullet OH$ formed from

600   heterogeneous Fenton's reaction on the catalyst surface. Other oxidants like $RuO_2(^\bullet OH)$ and

601   ClO^- also contributed to the decontamination, although with a less relevant role. The nano-

602   ZVI@C-N catalyst was composed of core-shell nanoparticles of 150-600 nm distributed along

603   N-doped carbon fusiform rods. It exhibited very good catalytic properties, along with: (i)

604   environmental compatibility because of the low toxicity of iron; (ii) high stability that ensures

605   its long service life, as deduced from the very low iron leaching at mild pH (0.20 mg L^{-1} at 50

606   mA); (iii) very efficient Fe(III)/Fe(II) redox cycling as a result of the abundance of nano-ZVI

607   upon synthesis at 800 ℃, as revealed by the low performance loss (10%) after 5 cycles; and

608   (iv) ferromagnetic properties, with high M_s and low coercive field that simplify its recovery

609   after use by employing a weak magnetic field. Cost analysis will be performed in future studies

610   at larger scale. The surface properties of the catalyst were analyzed by XRD and XPS and the

611   effect of key parameters on its catalytic activity was assessed via electrolysis in 0.050 M

612   Na_2SO_4 solutions at pH 5.5, which showed that its ability to degrade gemfibrozil was much

613   greater than that of the raw MOF and NH_2-MOF, and that of the calcined ZVI@C catalyst. GC-

614   MS analysis allowed the identification of twelve reaction products, whereas the kinetic analysis

615   of the drug concentration decays yielded the pseudo-first-order rate constants under different

616   conditions. The large mineralization observed and the gradual transformation of gemfibrozil

617   into aliphatic carboxylic acids ensured the detoxification.

622   **References**

623 [1] T.H. Miller, N.R. Bury, S.F. Owen, J.I. MacRae, L.P. Barron, Environ. Pollut. 239 (2018)

624 129-146.

625 [2] A.J. Ebele, M.A.-E. Abdallah, S. Harrad, Emerg. Contam. 3 (2017) 1-16.

626 [3] K. Kümmerer, Sustain. Chem. Pharm. 12 (2019) 100136.

627 [4] S. Bagnis, M.F. Fitzsimons, J. Snape, A. Tappin, S. Comber, Environ. Chem. Lett. 16

628 (2018) 1193-1216.

629 [5] K. Kümmerer, D.D. Dionysiou, O. Olsson, D. Fatta-Kassinos, Science 361 (6399) (2018)

630 222-224.

631 [6] M. Mezzelani, S. Gorbi, F. Regoli, Mar. Environ. Res. 140 (2018) 41-60.

632 [7] Time to get clean, Nature 526 (7572) (2015) 164.

633 [8] L. Feng, E.D. van Hullebusch, M.A. Rodrigo, G. Esposito, M.A. Oturan, Chem. Eng. J.

634 228 (2013) 944-964.

635 [9] E. Brillas, I. Sirés, TrAC-Trend. Anal. Chem. 70 (2015) 112-121.

636 [10] C.A. Martínez-Huitle, M.A. Rodrigo, I. Sirés, O. Scialdone, Chem. Rev. 115 (2015)

637 13362-13407.

638 [11] E. Brillas, I. Sirés, M.A. Oturan, Chem. Rev. 109 (2009) 6570-6631.

639 [12] M. Zhou, M.A. Oturan, I. Sirés, Springer Nature, Singapore (2018).

640 [13] M.H. Zhang, H. Dong, L. Zhao, D.X. Wang, D. Meng, Sci. Total Environ. 670 (2019)

641 110-121.

642 [14] N. Barhoumi, L. Labiadh, M.A. Oturan, N. Oturan, A. Gadri, S. Ammar, E. Brillas,

643 Chemosphere 141 (2015) 250-257.

644 [15] A. Galia, S. Lanzalaco, M.A. Sabatino, C. Dispenza, O. Scialdone, I. Sirés, Electrochem.

645 Commun. 62 (2016) 64-68.

646 [16] S. Lanzalaco, I. Sirés, M.A. Sabatino, C. Dispenza, O. Scialdone, A. Galia, Electrochim.

647 Acta 246 (2017) 812-822.

648   [17] T. Pérez, G. Coria, I. Sirés, J.L. Nava, A.R. Uribe, J. Electroanal. Chem. 812 (2018) 54-

649   58.

650   [18] Z. Ye, D.R.V. Guelfi, G. Álvarez, F. Alcaide, E. Brillas, I. Sirés, Appl. Catal. B: Environ.

651   247 (2019) 191-199.

652   [19] G. Coria, I. Sirés, E. Brillas, J.L. Nava, Chem. Eng. J. 304 (2016) 817-825.

653   [20] J.R. Steter, E. Brillas, I. Sirés, Appl. Catal. B: Environ. 224 (2018) 410-418.

654   [21] R. Salazar, M.A. Ureta-Zañartu, C. González-Vargas, C.D.N. Brito, C.A. Martínez-Huitle,

655   Chemosphere 198 (2018) 21-29.

656   [22] Z. Ye, J.R. Steter, F. Centellas, P.L. Cabot, E. Brillas, I. Sirés, J. Clean. Prod. 208 (2019)

657   1393-1402.

658   [23] S.O. Ganiyu, M. Zhou, C.A. Martínez-Huitle, Appl. Catal. B: Environ. 235 (2018) 103-

659   129.

660   [24] T.X.H. Le, M. Bechelany, M. Cretin, Carbon 122 (2017) 564-591.

661   [25] P. Su, M. Zhou, G. Ren, X. Lu, X. Du, G. Song, J. Mater. Chem. A 7 (2019) 24408-24419.

662   [26] D. Fernández, I. Robles, F.J. Rodríguez-Valadez, L.A. Godínez, Chemosphere 199 (2018)

663   251-255.

664   [27] A.J. dos Santos, I. Sirés, A.P.M. Alves, C.A. Martínez-Huitle, E. Brillas, Chemosphere

665   240 (2020) 124838.

666   [28] A.H. Ltaïef, S. Sabatino, F. Proietto, S. Ammar, A. Gadri, A. Galia, O. Scialdone,

667   Chemosphere 202 (2018) 111-118.

668   [29] X. Li, B. Wang, Y. Cao, S. Zhao, H. Wang, X. Feng, J. Zhou, X. Ma, ACS Sustainable

669   Chem. Eng. 7 (2019) 4548-4563.

670   [30] E. Dias, C. Petit, J. Mater. Chem. A. 3 (2015) 22484-22506.

671   [31] V.K. Sharma, M. Feng, J. Hazard. Mater. 372 (2019) 3-16.

672   [32] M. Cheng, C. Lai, Y. Liu, G. Zeng, D. Huang, C. Zhang, L. Qin, L. Hu, C. Zhou, W.

673   Xiong, Coord. Chem. Rev. 368 (2018) 80-92.

674   [33] H. Zhao, Y. Chen, Q. Peng, Q. Wang, G. Zhao, Appl. Catal. B: Environ. 203 (2017) 127-

675   137.

676   [34] T.X.H. Le, M.G. Cowan, M. Drobek, M. Bechelany, A. Julbe, M. Cretin, Nanomaterials,

677   9 (2019) 641.

678   [35] K. Liu, M. Yu, H. Wang, J. Wang, W. Liu, M.R. Hoffmann, Environ. Sci. Technol. 53

679   (2019) 6474-6482.

680   [36] T.X.H. Le, R. Esmilaire, M. Drobek, M. Bechelany, C. Vallicari, D.L. Nguyen, A. Julbe,

681   S. Tingry, M. Cretin, J. Mater. Chem. A 4 (2016) 17686-17693.

682   [37] T.X.H. Le, R. Esmilaire, M. Drobek, M. Bechelany, C. Vallicari, S. Cerneaux, A. Julbe,

683   M. Cretin, J. Phys. Chem. C 121 (2017) 15188-15197.

684   [38] C. Gao, S. Chen, X. Quan, H. Yu, Y. Zhang, J. Catal. 356 (2017) 125-132.

685   [39] T. Zeng, M.D. Yu, H.Y. Zhang, Z.Q. He, J.M. Chen, S. Song, Catal. Sci. Technol. 7 (2017)

686   396-404.

687   [40] A. Banerjee, R. Gokhale, S. Bhatnagar, J. Jog, M. Bhardwaj, B. Lefez, B. Hannoyer, S.

688   Ogale, J. Mater. Chem. 22 (2012) 19694-19699.

689   [41] K.Y. Andrew Lin, F.K. Hsu, RSC Adv. 5 (2015) 50790-50800.

690   [42] W. Li, X. Wu, S. Li, W. Tang, Y. Chen, Appl. Surf. Sci. 436 (2018) 252-262.

691   [43] J.T. Tang, J.L. Wang, Chem. Eng. J. 351 (2018) 1085-1094.

692   [44] Z. Wang, J. Yang, Y. Li, Q. Zhuang, J. Gu, Eur. J. Inorg. Chem. 2018 (2018) 23-30.

693   [45] Y. Wu, X. Chen, Y. Han, D. Yue, X. Cao, Y. Zhao, X. Qian, Environ. Sci. Technol. 53

694   (2019) 9081-9090.

695   [46] L. Shi, T. Wang, H. Zhang, K. Chang, X. Meng, H. Liu, J. Ye, Adv. Sci. 2 (2015) 1500006.

696 [47] C. Liu, Y. Wang, Y. Zhang, R. Li, W. Meng, Z. Song, F. Qi, B. Xu, W. Chu, D. Yuan, B.

697   Yu, Chem. Eng. J. 354 (2018) 835-848.

698 [48] F. Desbiolles, L. Malleret, C. Tiliacos, P. Wong-Wah-Chung, I. Laffont-Schwob, Sci.

699   Total Environ. 639 (2018) 1334-1348.

700 [49] P. Grenni, L. Patrolecco, N. Ademollo, M. Di Lenola, A.B. Caracciolo, Microchem. J.

701   136 (2018) 49-55.

702 [50] T. Deblonde, C. Cossu-Leguille, P. Hartemann, Int. J. Hyg. Environ. Health 214 (2011)

703   442-448.

704 [51] Y. Fang, A. Karnjanapiboonwong, D.A. Chase, J. Wang, A.N. Morse, T.A. Anderson,

705   Environ. Toxicol. Chem. 31 (2012) 550-555.

706 [52] M. Isidori, M. Bellotta, M. Cangiano, A. Parrella, Environ. Int. 35 (2009) 826-829.

707 [53] G. Lee, S. Lee, N. Ha, Y. Kho, K. Parkd, P. Kimd, B. Ahne, S. Kima, K. Choi, Ecotoxicol.

708   Environ. Saf. 173 (2019) 174-181.

709 [54] E. Cuervo Lumbaque, R.M. Cardoso, A. Dallegrave, L.O. dos Santos, M. Ibáñez, F.

710   Hernández, C. Sirtori, J. Environ. Chem. Eng. 6 (2018) 3951-3961.

711 [55] V.A.B. Paiva, C.E.S. Paniagua, I.A. Ricardo, B.R. Gonçalves, S.P. Martins, D. Daniel,

712   A.E.H. Machado, A.G. Trovó, J. Environ. Chem. Eng. 6 (2018) 1086-1092.

713 [56] C.E.S. Paniagua, I.A. Ricardo, E.O. Marson, B.R. Gonçalves, A.G. Trovó, J. Environ.

714   Chem. Eng. 7 (2019) 103164.

715 [57] W. Yao, X. Wang, H. Yang, G. Yu, S. Deng, J. Huang, B. Wang, Y. Wang, Water Res.

716   88 (2016) 826-835.

717 [58] O. Rodríguez-Nava, H. Ramírez-Saad, O. Loera, I. González, Environ. Technol. 37 (2016)

718   2964-2974.

719 [59] M. Ma, H. Noei, B. Mienert, J. Niesel, E. Bill, M. Muhler, R.A. Fischer, Y. Wang, U.

720   Schatzschneider, N. Metzler-Nolte, Chem. Eur. J. 19 (2013) 6785-6790.

721   [60] M. Pu, Y. Ma, J. Wan, Y. Wang, J. Wang, M.L. Brusseau, Catal. Sci. Technol. 7 (2017)

722   1129-1140.

723   [61] J. Wang, D. Chen, B. Li, J. He, D. Duan, D. Shao, M. Nie, Sci. Rep. 6 (2016) 26126.

724   [62] M. Angamuthu, G. Satishkumar, M.V. Landau, Micropor. Mesopor. Mater. 251 (2017)

725   58-68.

726   [63] P. Zhao, X. Hua, W. Xu, W. Luo, S. Chen, G. Cheng, Catal. Sci. Technol. 6 (2016) 6365-

727   6371.

728   [64] S.-H. Zhang, M.-F. Wu, T.-T. Tang, Q.-J. Xing, C.-Q. Peng, F. Li, H. Liu, X.-B. Luo, J.-

729   P. Zou, X.-B. Min, J.-M. Luo, Chem. Eng. J. 335 (2018) 945-953.

730   [65] B.S. Girgis, Y.M. Temerk, M.M. Gadelrab, I.D. Abdullah, Carbon Sci. 8 (2007) 95-100.

731   [66] E.M. Peña-Méndez, R.M. Mawale, J.E. Conde-González, B. Socas-Rodríguez, J. Havel,

732   C. Ruiz-Pérez, Talanta 207 (2020) 120275.

733   [67] K. Rohith Vinod, P. Saravanan, M. Sakar, S. Balakumar, RSC Adv. 6 (2016) 45850.

734   [68] D.H. Bremner, A.E. Burgess, D. Houllemare, K.-C. Namkung, Appl. Catal. B: Environ.

735   63 (1-2) (2006) 15-19.

736   [69] Z. Ye, E. Brillas, F. Centellas, P.L. Cabot, I. Sirés, Water Res. 169 (2020) 115219.

737   [70] A. Bianco, M.I. Polo-López, P. Fernández-Ibánez, M. Brigante, G. Mailhot, Water Res.

738   118 (2017) 246-260.

739   [71] P. Chen, F. Wang, Z.-F. Chen, Q. Zhang, Y. Su, L. Shen, K. Yao, Y. Liu, Z. Cai, W. Lv,

740   G. Liu, Appl. Catal. B: Environ. 204 (2017) 250-259.

741

Figure captions

Fig. 1. XRD patterns of (a) the as-synthesized MIL(Fe)-type (*a*) and NH$_2$-MIL(Fe)-type MOFs (*b*), and (b) the nano-ZVI@C (*a'*) and nano-ZVI@C-N (*b'*) catalysts obtained upon calcination at 800 ºC, respectively.

Fig. 2. (a,b,c,d) TEM analysis and (e) site of interest along with EDS elemental mapping showing the distribution of Fe, O, N and C for the nano-ZVI@C-N catalyst obtained upon calcination at 800 ºC.

Fig. 3. Magnetization curve recorded at 300 K for the nano-ZVI@C-N catalyst obtained upon calcination at 800 ºC. The inset shows a magnified view from -2000 to 2000 Oe.

Fig. 4. Normalized gemfibrozil concentration decay with electrolysis time during the (△,□) adsorption and (▲,■) EF treatments of 150 mL of drug solutions (10 mg C L^{-1}) with 0.050 M Na$_2$SO$_4$ at natural pH 5.5 and 35 ºC using 0.2 g L^{-1} of catalysts prepared by calcination at 800 ºC. Two types of catalysts were employed: (△,▲) nano-ZVI@C (derived from MIL(Fe)-type MOF) and (□,■) nano-ZVI@C-N (derived from NH$_2$-MIL(Fe)-type MOF). For comparison, the trends for (×) EO-H$_2$O$_2$ (no catalyst) and (●) EF with raw NH$_2$-MIL(Fe)-type catalyst are also shown. EO-H$_2$O$_2$ and EF trials were carried out with an IrO$_2$/air-diffusion cell at 50 mA.

Fig. 5. (a) Normalized gemfibrozil concentration vs. electrolysis time during the EF treatment of 150 mL of drug solutions (10 mg C L^{-1}) with 0.050 M Na$_2$SO$_4$ at natural pH 5.5 and 35 ºC in an IrO$_2$/air-diffusion cell at 50 mA, using 0.2 g L^{-1} of nano-ZVI@C-N catalyst prepared by pyrolysis at different temperatures: (●) 650 ºC, (▲) 700 ºC, (■) 800 ºC and (◆) 900 ºC. (b) Pseudo-first-order kinetic analysis of the drug decay concentration in the two latter trials.

Fig. 6. Normalized gemfibrozil concentration decay versus electrolysis time during the EF treatment of 150 mL of drug solutions (10 mg C L^{-1}) with 0.050 M Na$_2$SO$_4$ at 35 ºC in an

765   IrO$_2$/air-diffusion cell using the nano-ZVI@C-N catalyst synthesized by calcination at 800 ºC.

766   (a) Effect of initial pH, using 0.2 g L^{-1} of catalyst at 50 mA. pH: (●) 3.0, (■) 5.5 (natural), (▲)

767   7.0 and (◆) 9.0. (b) Effect of applied current, using 0.2 g L^{-1} of catalyst at natural pH 5.5. I:

768   (●) 25 mA, (■) 50 mA, (▲) 75 mA and (◆) 100 mA. (c) Effect of catalyst dosage, at natural

769   pH 5.5 and 50 mA. Catalyst concentration: (●) 0.05 g L^{-1}, (▲) 0.1 g L^{-1}, (■) 0.2 g L^{-1} and (◆)

770   0.3 g L^{-1}.

771   **Fig. 7.** Normalized gemfibrozil concentration with electrolysis time during the EF treatment of

772   150 mL of drug solutions (10 mg C L^{-1}) at pH 5.5, 50 mA and 35 ºC using 0.2 g L^{-1} of the nano-

773   ZVI@C-N catalyst prepared by calcination at 800 ºC. Different anodes (coupled to an air-

774   diffusion cathode) and electrolytes (with the same total specific conductivity) were employed:

775   (▼) IrO$_2$ anode with 0.041 M Na$_2$SO$_4$ + 0.009 M NaHCO$_3$, (■) IrO$_2$ anode with 0.050 M

776   Na$_2$SO$_4$, (◣) BDD anode with 0.050 M Na$_2$SO$_4$ and (◢) RuO$_2$ anode with 0.025 M Na$_2$SO$_4$ +

777   0.035 M NaCl.

778   **Fig. 8.** Proposed degradation route of gemfibrozil solutions at mild pH by heterogeneous EF

779   with the nano-ZVI@C-N catalyst using a BDD/air-diffusion cell.

780   **Fig. 9.** Normalized concentration decay vs electrolysis time during the EF process of 150 mL

781   of a mixture of (■) gemfibrozil, (○) bisphenol A, (▽) naproxen and (▷) fluoxetine (each at

782   10 mg C L^{-1}), spiked into conditioned urban wastewater at pH 7.0 and 35 ºC in a RuO$_2$/air-

783   diffusion cell, at 50 mA using 0.2 g L^{-1} of the nano-ZVI@C-N catalyst synthesized by

784   calcination at 800 ºC.

785   **Fig. 10.** Proposed mechanism for the nano-ZVI@C-N-catalyzed heterogeneous EF treatment

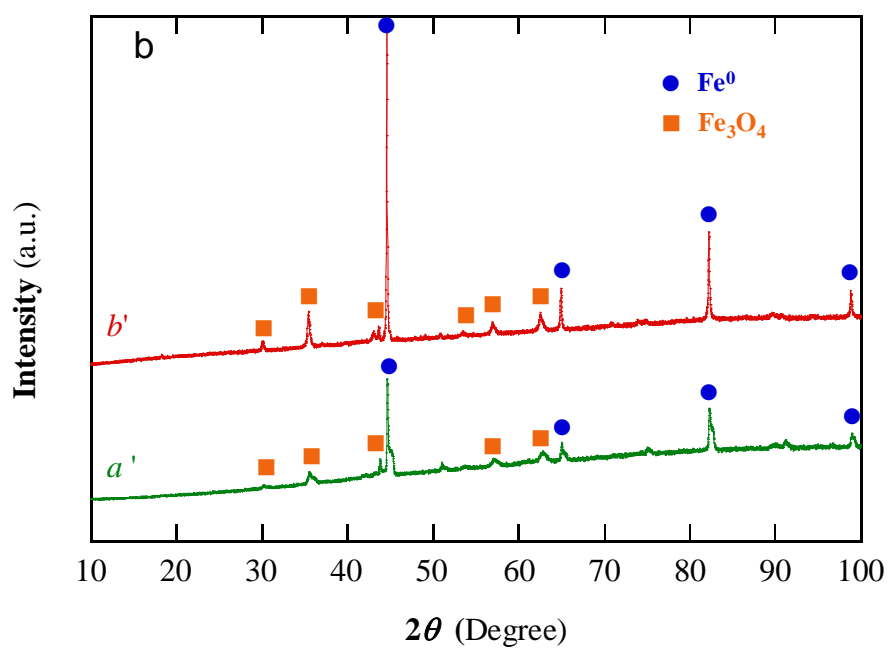786   of gemfibrozil solutions at mild pH.
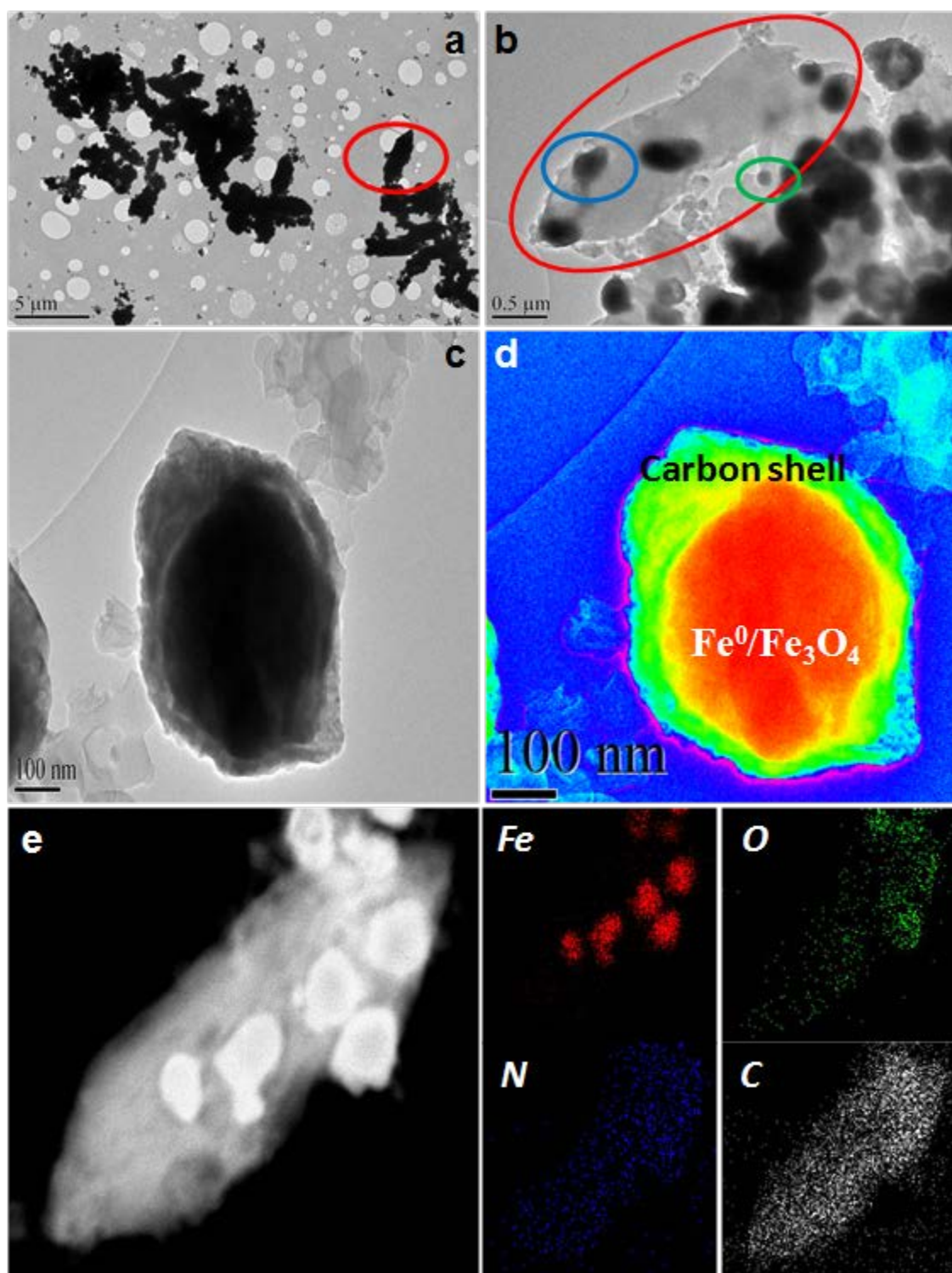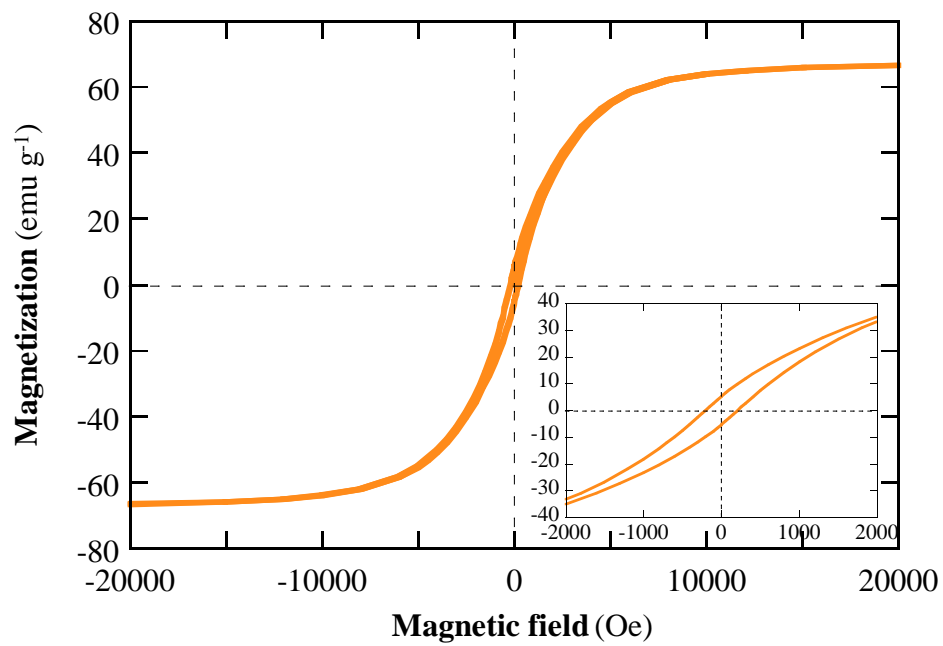
787

788

789

790

791

792

793

Fig. 1

795

796
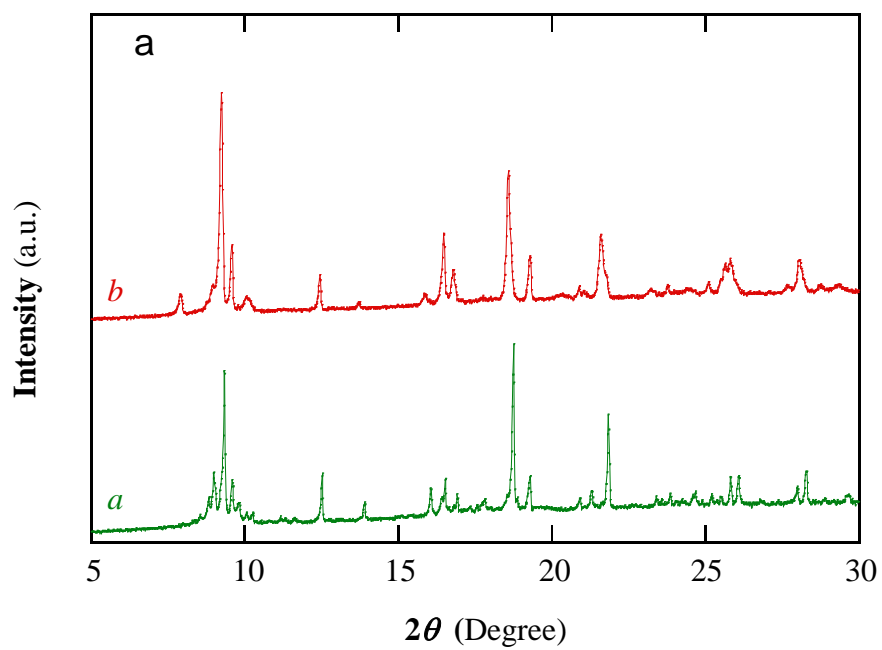
797

798

799

800   **Fig. 2**

801

802

803

804

805
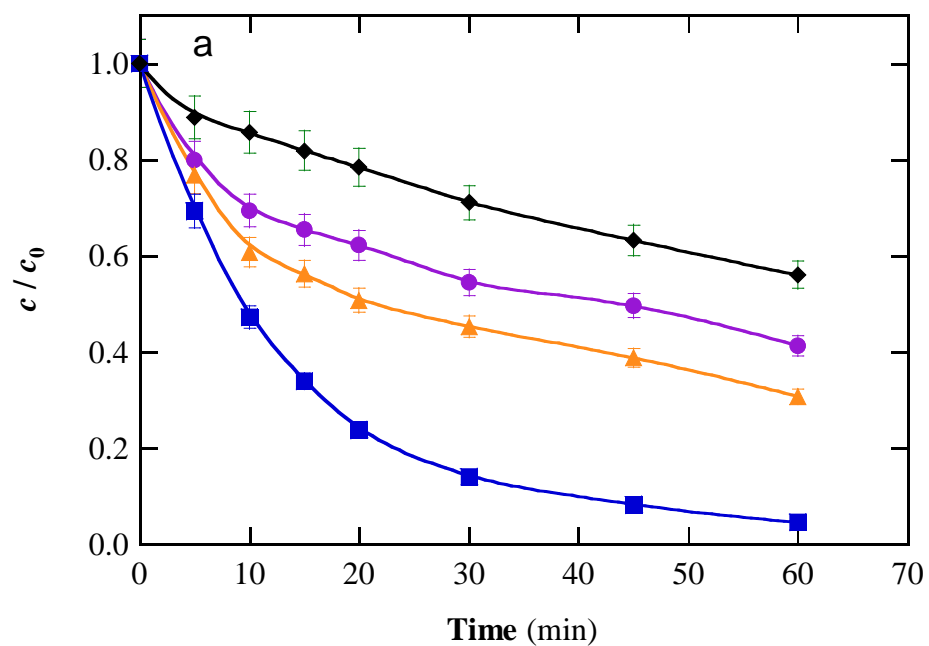
806

Fig. 3

807

808

809

810

811

812
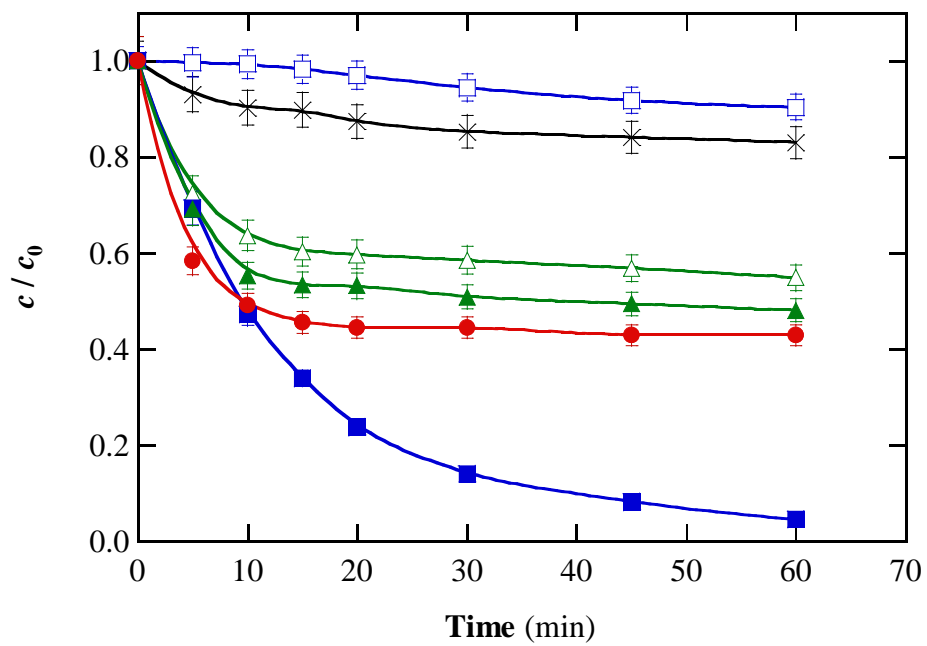
Fig. 4

814

815

816
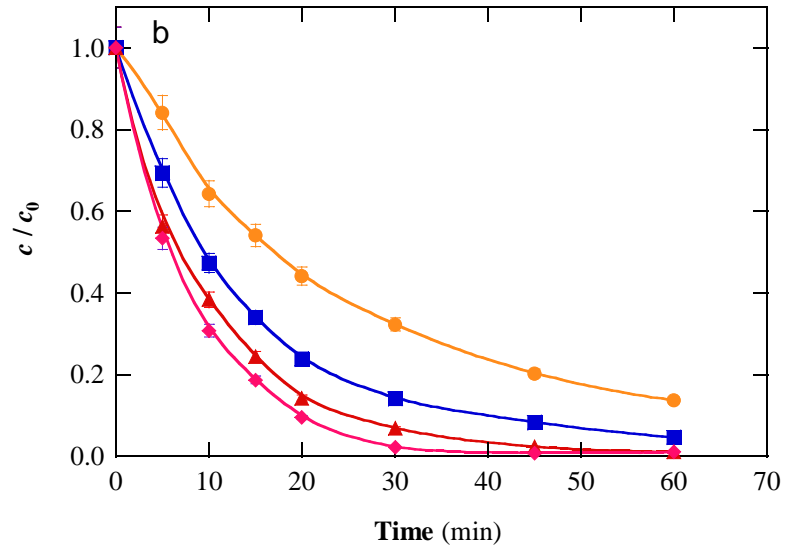

817

818

819

820

821

Fig. 5

822
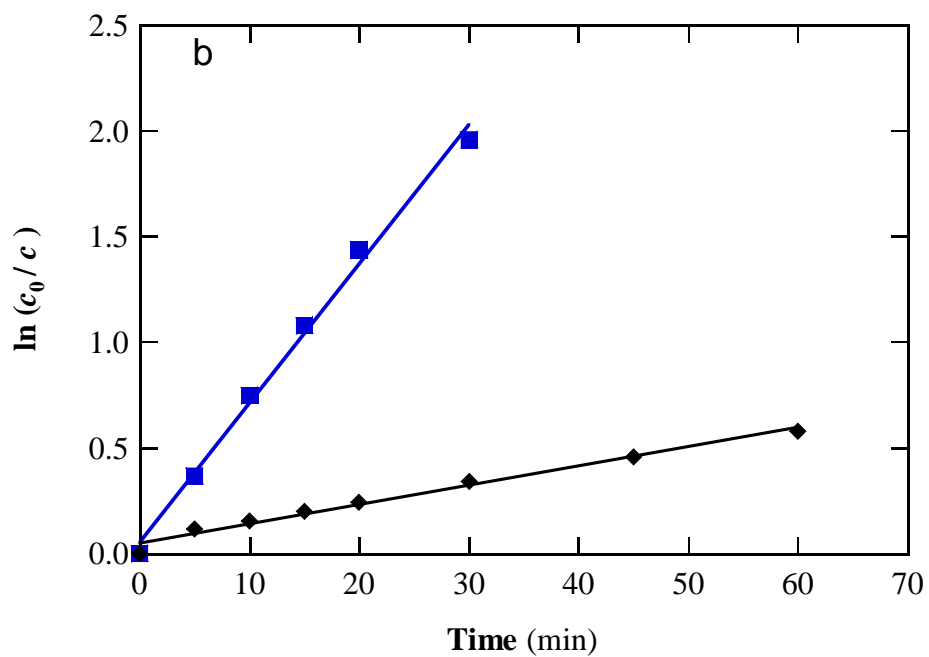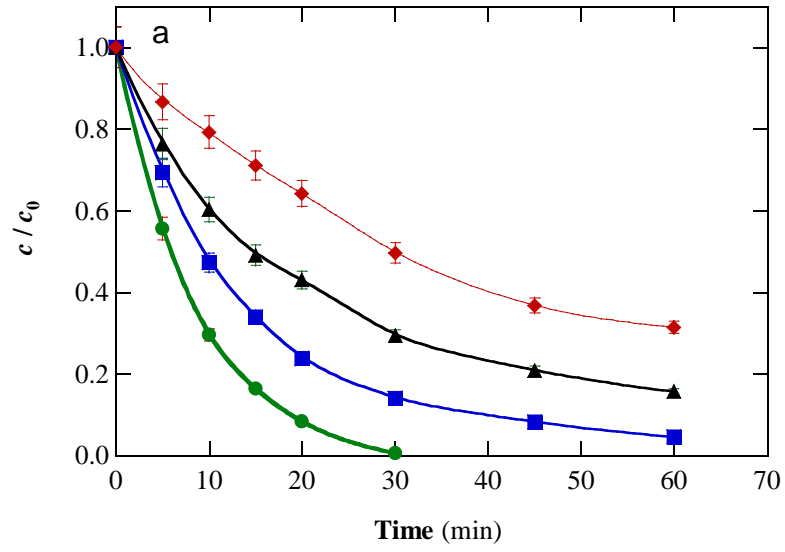
823

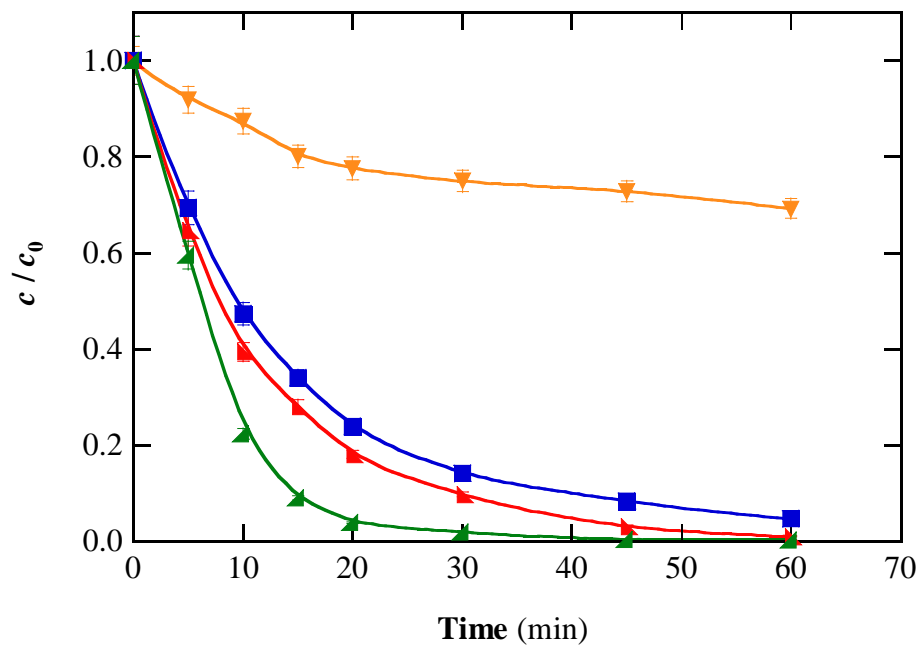
824
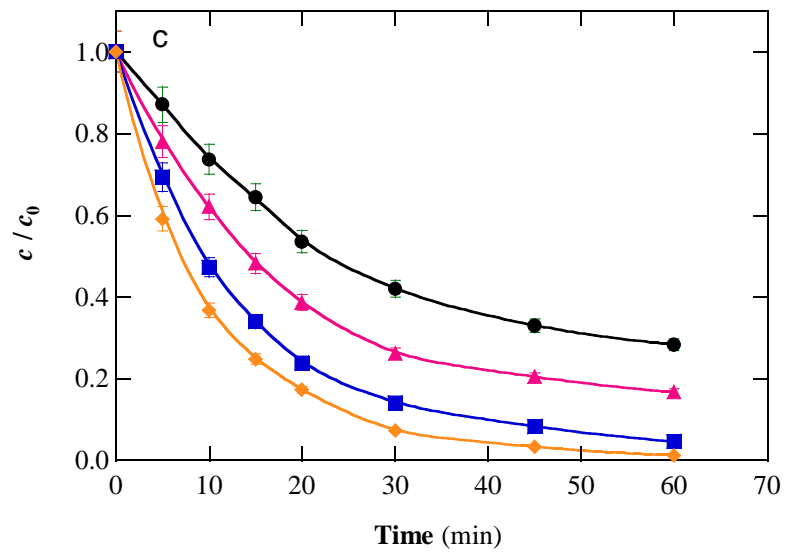
825

826

Fig. 6

827

828

829

830

831

832   **Fig. 7**
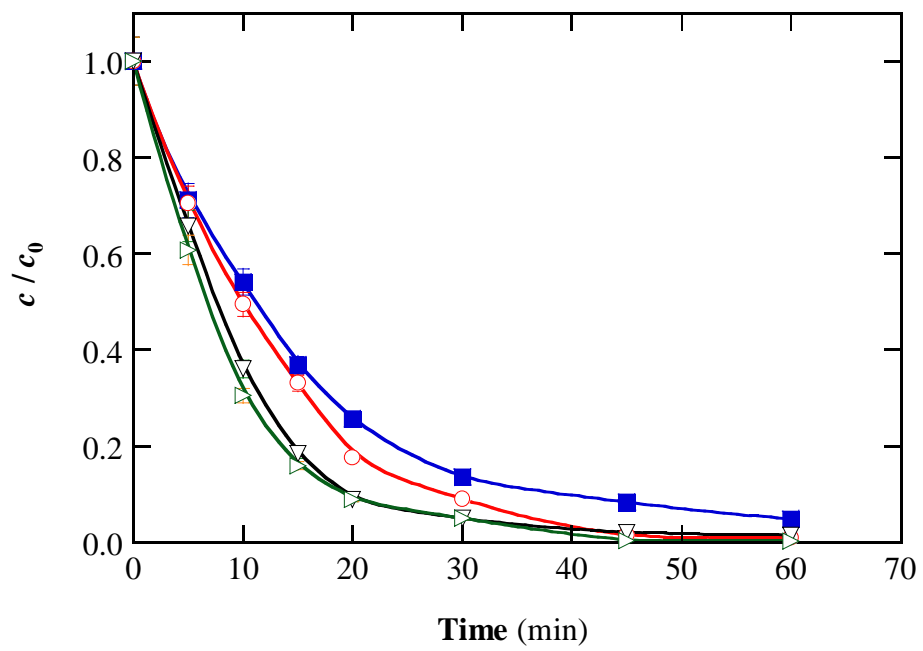
833
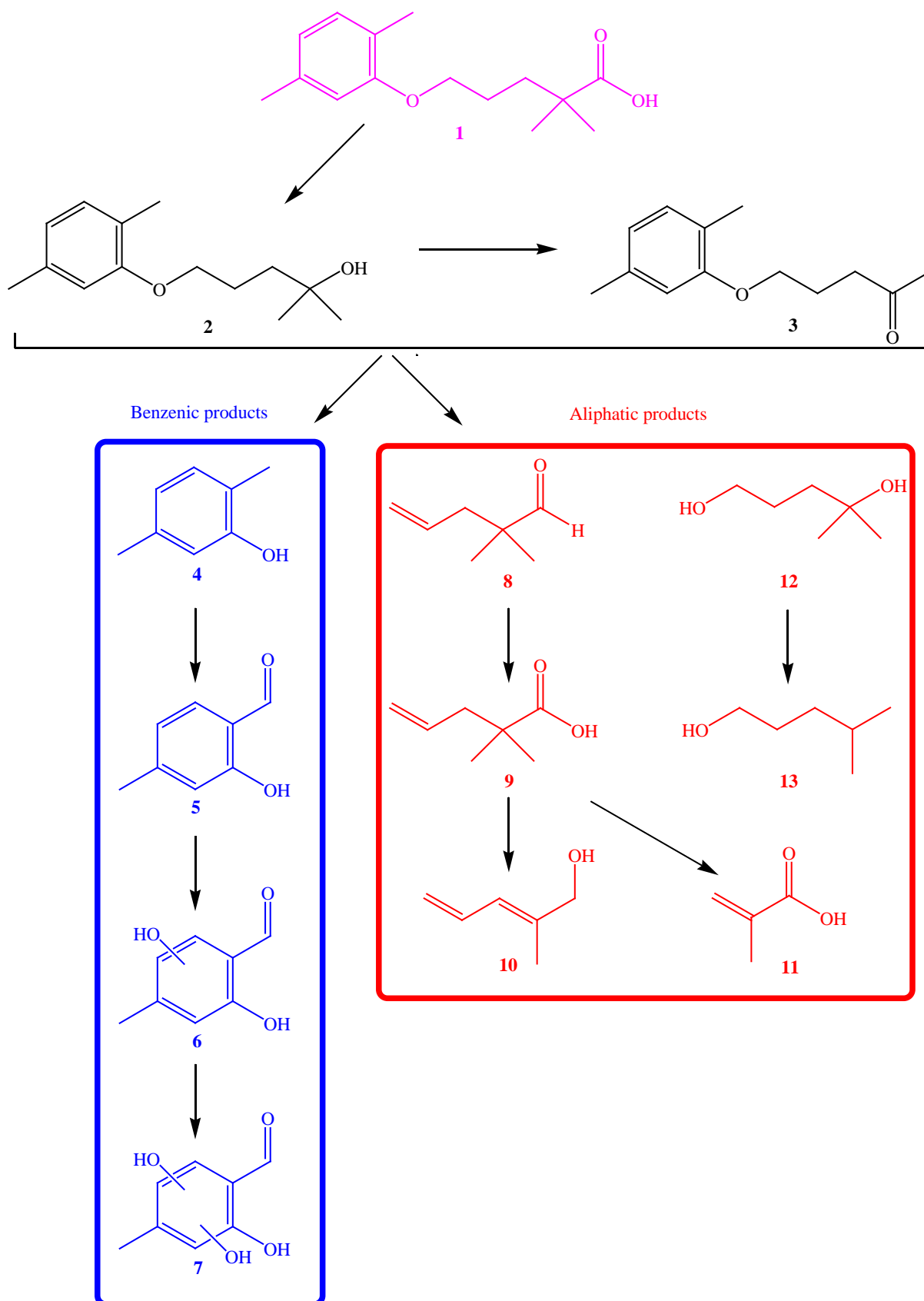
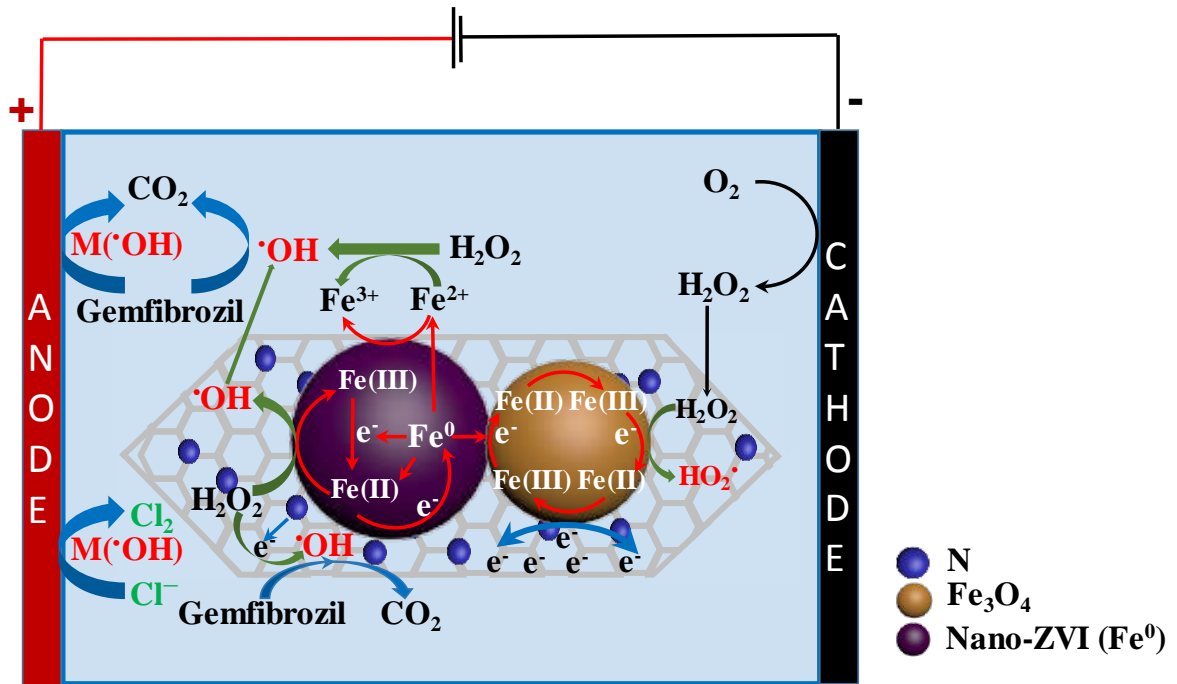**Fig. 8**

837

838

839

840

841

Fig. 9

843

844

845

846

847

Fig. 10

849

850   **Table 1.**

851   Pseudo-first-order rate constants and R-squared values obtained for the gemfibrozil

852   concentration decay during the EF treatment of 150 mL of drug solutions (10 mg C L^{-1}) in 0.050

853   M Na$_2$SO$_4$ at 35 ℃ using an IrO$_2$/air-diffusion cell with a nano-ZVI@C-N catalyst synthesized

854   by calcination at 800 ℃.

pH	I (mA)	[Catalyst] (g L^{-1})	k_1 (min^{-1})	R^2
3.0	50	0.2	0.1239	0.999
5.5 (natural)	25	0.2	0.0333	0.991
	50	0.05	0.0295	0.997
	50	0.1	0.0450	0.997
	50	0.2	0.0659	0.993
	50	0.3	0.0860	0.997
	75	0.2	0.0894	0.995
	100	0.2	0.1154	0.998
7.0	50	0.2	0.0400	0.989
9.0	50	0.2	0.0198	0.987

855